

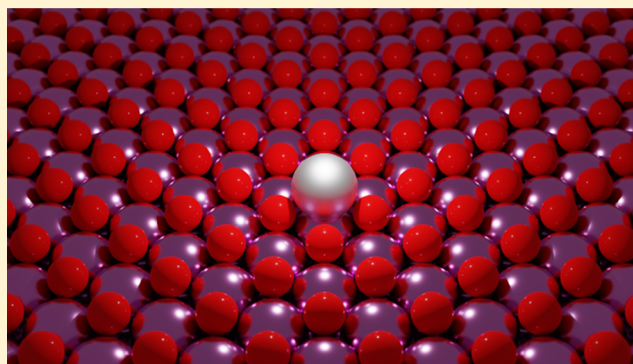
# Predicting Metal–Support Interactions in Oxide-Supported Single-Atom Catalysts

Kaiyang Tan, Mudit Dixit,<sup>ID</sup> James Dean, and Giannis Mpourmpakis\*<sup>ID</sup>

Department of Chemical Engineering, University of Pittsburgh, Pittsburgh, Pennsylvania 15261, United States

## Supporting Information

**ABSTRACT:** Single-atom catalysts (SACs), containing under-coordinated single metal atoms bound to the surface of supports, are promising heterogeneous catalysts due to their intrinsic catalytic properties and efficient utilization of noble metal atoms. However, SAC stability under catalytic operation is questioned due to the tendency of metals to sinter (aggregation). Herein, we perform density functional theory (DFT) calculations to investigate the metal–support interactions (MSIs) of a series of transition-metal atoms supported on three common oxide supports ( $\gamma\text{-Al}_2\text{O}_3$ ,  $\text{MgO}$ , and  $\text{MgAl}_2\text{O}_4$ ). Moreover, utilizing the DFT results and genetic programming, we develop a predictive model for the strength of MSIs using simple properties of both the SACs and supports. Finally, we introduce criteria for the synthetic accessibility of SACs based on thermodynamic arguments. Our computational work can guide experiments by identifying combinations of metals and oxides that can potentially lead to highly stable (and catalytically durable) SACs.



## INTRODUCTION

Catalysts play a central role in various chemical and biological transformations by controlling the rates of both desired and undesired reactions.<sup>1–3</sup> Among different homogeneous and heterogeneous catalysts, due to their ability to change oxidation states and form complexes, transition-metal nanoparticles (TMNPs) find tremendous application in catalysis.<sup>4–6</sup> Since catalytic reactions occur at the surface of TMNP-based catalysts, only the surface metal atoms can be utilized as active sites. As a result, the subsurface atoms of TMNPs are essentially wasted and introduce an extra economic cost to industrial processes.<sup>2,5</sup> To maximize the ratio of exposed metal atoms, an obvious solution is to make the TMNP as small as possible. Efforts to reduce TMNP size have led to the development of single-atom catalysts (SACs). SACs are a new frontier in catalysis designed to address the issue of atom economy: the metal is atomically dispersed on the support, making all atoms accessible for catalysis.<sup>2,5–9</sup> Due to the under-coordination of the metal, quantum size effects, and strong metal–support interactions (MSIs),<sup>6,7</sup> SACs can exhibit high catalytic activity and selectivity in a wide range of chemical transformations.<sup>6,8</sup> Recently, a series of noble metal SACs were synthesized and characterized in a variety of supports.<sup>10–19</sup> For instance,  $\text{Pd}_1/\text{MgO}(100)$  synthesized by high-frequency laser evaporation shows a unique size effect: the Pd cluster size governs the reacting temperature and mechanism of the catalyzed cyclo-trimerization of acetylene to benzene.<sup>20</sup>  $\text{Pt}_1/\text{graphene}$  has been successfully synthesized by atomic layer deposition and exhibits a high activity for methanol oxidation

with superior tolerance for CO. This catalyst has excellent performance due to low-coordination and the presence of unsaturated 5d orbitals on the single Pt atom.<sup>21</sup>  $\text{Rh}/\text{ZnO}$  nanowires have been fabricated via the facile adsorption method. When catalyzing the hydroformylation of olefins, these nanowires exhibit orders of magnitude higher activity than typical heterogeneous catalysts.<sup>22</sup> A well-known SAC is  $\text{Ir}_1/\text{FeO}_x$ , whose water–gas shift activity is an order of magnitude higher than on TMNP.<sup>23</sup> Related to SACs are catalysts based on site pairs, where two isolated atoms form an active catalytic site. In 2018, Guan and Gates demonstrated Rh site pairs on  $\text{MgO}$  to catalyze the hydrogenation of ethylene and hydrogen–deuterium exchange with higher activity compared to isolated Rh sites.<sup>24</sup> Similarly, Wang et al. recently showed that Pt atoms could form  $\text{Pt}-\text{O}-\text{Pt}$  site pairs on  $\text{CeO}_2$ , with enhanced low-temperature CO oxidation activity compared to single Pt sites. Overall, although SACs do not universally deliver improved activities versus larger catalysts (e.g., nanoparticles and clusters), they show great promise in catalyzing a variety of reactions.<sup>11,20,23</sup> However, their penetration into the industrial sector has been slowed<sup>2</sup> by the need for improved characterization methodologies,<sup>25</sup> a lack of scalable, cost-effective synthetic techniques, and stability

Received: July 24, 2019

Revised: October 4, 2019

Accepted: October 8, 2019

Published: October 8, 2019

issues, which result in the agglomeration of SACs into larger particles.<sup>26</sup>

Due to the strong cohesive energy and unfavorable surface energy of single transition-metal atoms, the active metals of SACs have the thermodynamic tendency to sinter, which raises questions regarding the stability of SACs under realistic catalytic conditions.<sup>27–29</sup> Sintering of SACs reduces their catalytic activity<sup>30–32</sup> by reducing the surface area and increasing the average coordination of the metal atoms.<sup>33</sup> However, strong MSIs can mitigate sintering by anchoring metals to the support,<sup>34</sup> stabilizing the SACs, and preserving their high surface area. For instance, in the case of Pt<sub>1</sub>/FeO,<sup>x</sup> despite the high surface free energies of single Pt atoms, the Pt atoms are stabilized on the support via the formation of Pt–O–Fe metal–support bonds.<sup>23</sup> It has also been shown that the MSIs can dictate the performance of SACs, making it feasible to tune their activity, selectivity, and stability during catalytic operation.<sup>35–37</sup> In recent years, a number of research efforts have focused on characterizing MSIs through both experiment (such as utilizing aberration-corrected environmental TEM chambers to dynamically study MSIs<sup>38</sup>) and computation (using DFT and statistical learning to generate predictive models<sup>39</sup>). Despite these advances, a fundamental understanding of the primary interactions in SACs is still lacking. To understand MSIs, one needs to identify simple descriptors for the strength of MSI, ideally based on fundamental physical properties of the supported metal atoms and the supports. Several outstanding contributions have demonstrated linear scaling relationships between metal adsorption energy and metal–support pair properties (for SACs and other supported TMNPs) such as surface energy of the metal, metal oxidation enthalpy,<sup>40</sup> the heat of metal oxide formation,<sup>41</sup> and support reducibility.<sup>42</sup> These findings suggest that MSIs are influenced by the properties of both the metal and the support. Using DFT, O'Connor et al.<sup>39</sup> confirmed the metal oxidation enthalpy and support reducibility to be descriptors for metal adsorption in the case of SACs. They demonstrated that both metal and oxygen atoms on the support surface contribute to adsorption. Furthermore, they applied statistical learning methods to build predictive models by including various metal–support properties and investigated a large set of descriptors for SAC adsorption energy.

In this work, we calculate the adsorption energies of a series of metal atoms spanning different columns and rows in the periodic table (Au, Cu, Ag, Pt, Pd, Ni, Rh, and Ir) on low-index surface facets of three oxides ( $\gamma$ -Al<sub>2</sub>O<sub>3</sub>(100),  $\gamma$ -Al<sub>2</sub>O<sub>3</sub>(110),  $\gamma$ -Al<sub>2</sub>O<sub>3</sub>(111), MgO(100), MgO(110), MgAl<sub>2</sub>O<sub>4</sub>(100), and MgAl<sub>2</sub>O<sub>4</sub>(110)) that are commonly used as supports in catalysis. We identify two primary descriptors for MSIs (quantified in this work as adsorption energy), namely, the gas-phase metal–oxygen binding energy ( $E_{M-O}$ ) and the band gap of the oxide support. By using the DFT results as a training set for genetic programming, we develop a predictive model for the adsorption energy of metals on supports. Finally, we apply the square-root bond (SRB) cutting model<sup>43,44</sup> to introduce a thermodynamics-based guiding principle for the synthetic accessibility of SACs. This computational framework can potentially aid the synthesis of highly stable SACs by identifying metal and support combinations that exhibit strong MSI.

## METHODS

DFT calculations were performed using CP2K.<sup>45</sup> The Perdew–Burke–Ernzerhof (PBE) exchange-correlation functional<sup>46</sup> was used in combination with Grimme's D3 dispersion-correction method<sup>47</sup> to account for long-range MSIs. Dipole corrections<sup>48</sup> were also added to accurately investigate asymmetric slab systems. TZVP basis sets<sup>49</sup> were used for O; DZVP basis sets<sup>49</sup> were used for Al, Mg, Au, Cu, Ag, Pt, Pd, Ni, Rh, and Ir. Additionally, we use the pseudopotentials of Goedecker, Teter, and Hutter<sup>50–52</sup> with a kinetic energy cutoff 400 Ry. For the oxide bulk optimizations, we used a  $1 \times 1 \times 1$  "supercell" for  $\gamma$ -Al<sub>2</sub>O<sub>3</sub> and MgAl<sub>2</sub>O<sub>4</sub> due to their already-large unit cell and a  $2 \times 2 \times 2$  supercell for MgO. Following optimization of the bulk, we cleave the supercells to construct slabs. We use a  $2 \times 1$  slab with 2 layers of repeating supercell for  $\gamma$ -Al<sub>2</sub>O<sub>3</sub>, a  $1 \times 1$  slab with 1 layer of repeating supercell for MgO, and a  $2 \times 1$  slab with 1 layer of repeating supercell for MgAl<sub>2</sub>O<sub>4</sub>.  $\gamma$ -Al<sub>2</sub>O<sub>3</sub> and MgAl<sub>2</sub>O<sub>4</sub> had a vacuum distance of 10 Å between repeating slabs, and MgO had a vacuum distance of 15 Å (the periodic box size for each slab can be found in Table S1). The two bottom atomic layers were fixed in their cell positions. Systems were relaxed with a force-convergence criterion of 0.0004 Ha/bohr and an SCF convergence criterion of  $10^{-8}$  Ha. The metal adsorption energy ( $E_{ads}$ ) is calculated by eq 1, where  $E_{M-support}$  is the total energy of the metal–support system,  $E_{support}$  is the energy of the support, and  $E_M$  is the gas-phase energy of the single metal atom.

$$E_{ads} = E_{M-support} - E_{support} - E_M \quad (1)$$

To calculate the metal–oxygen binding energy ( $E_{M-O}$ ) accurately (listed in Table S4 of the Supporting Information), we calculated the energy of a gas-phase metal binding with a single oxygen atom. To accurately access the energies, we investigated several different spin states and chose the minimum-energy spin state of the metal–oxygen complex (listed in Table S4 of the Supporting Information).

## RESULTS AND DISCUSSION

To examine the MSIs, we studied the adsorption of single metal atoms on  $\gamma$ -Al<sub>2</sub>O<sub>3</sub>, MgO, and MgAl<sub>2</sub>O<sub>4</sub>, which are both thermally stable and commonly used as supports in catalysis.<sup>53–55</sup> In these oxides, the surface Lewis acid–base properties for under-coordinated site pairs benefit charge transfer when metal atoms adsorb on the surface.<sup>56–59</sup> Because of their ubiquity as supports, a series of SACs have already been synthesized, including Pt<sub>1</sub>/ $\gamma$ -Al<sub>2</sub>O<sub>3</sub>,<sup>60</sup> Rh<sub>1</sub>/ $\gamma$ -Al<sub>2</sub>O<sub>3</sub>,<sup>4,61</sup> Au<sub>1</sub>/MgO,<sup>62</sup> Pd<sub>1</sub>/MgO,<sup>20</sup> and Ir<sub>1</sub>/MgAl<sub>2</sub>O<sub>4</sub>.<sup>63</sup> Different surface facets of metal oxides exhibit different surface coordination, so we investigate a variety of low-index surface facets:  $\gamma$ -Al<sub>2</sub>O<sub>3</sub>(100),  $\gamma$ -Al<sub>2</sub>O<sub>3</sub>(110),  $\gamma$ -Al<sub>2</sub>O<sub>3</sub>(111), MgO(100), MgO(110), MgAl<sub>2</sub>O<sub>4</sub>(100), and MgAl<sub>2</sub>O<sub>4</sub>(110). Depending on the offset of the termination plane from the origin of the unit cell, each crystallographic facet can be terminated with different atoms. Therefore, we screen multiple surface terminations for each facet and report the most thermodynamically stable surfaces, because they likely represent a significant portion of the exposed surface area.

The MgO(111) and MgAl<sub>2</sub>O<sub>4</sub>(111) surfaces exhibit high net dipole due to their asymmetric nature, which results in high energy regardless of termination. In addition, they undergo severe restructuring (indicative of unstable surfaces), so we do

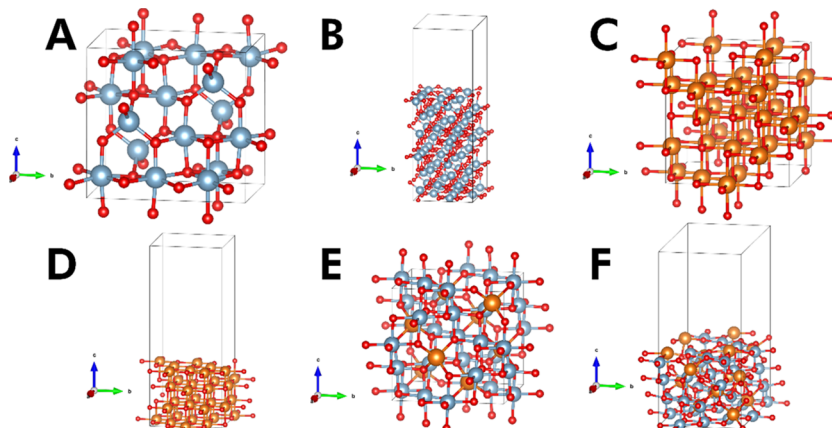


**Figure 1.** Structures of (a)  $\gamma\text{-Al}_2\text{O}_3$  bulk, (b)  $\gamma\text{-Al}_2\text{O}_3(100)$  facet, (c) MgO bulk, (d) MgO(100) facet, (e)  $\text{MgAl}_2\text{O}_4$  bulk, and (f)  $\text{MgAl}_2\text{O}_4(100)$  facet. Orange atoms represent Mg, gray atoms represent Al, and red atoms represent O.

not include them in this study. The optimized bulk structures and the most stable facets of the considered oxide supports are shown in Figure 1. The other facets are shown in Figure S1 of the Supporting Information.

Following optimization of the different surfaces, we placed the single metal atoms on different sites. Depending on the heterogeneity of the oxide surface, several metal adsorption sites may be possible. The initial guess for the metal adsorption site is selected to maximize the interaction of the metal atom with neighboring surface oxygen atoms, because many of the metal atoms we select are oxophilic in nature. We investigate 4 adsorption sites on  $\gamma\text{-Al}_2\text{O}_3(100)$  and (111) (Figure 2a,c), 5 sites on  $\gamma\text{-Al}_2\text{O}_3(110)$  (Figure 2b), 1 site on MgO(100) and (110) (Figure 2d,e), 3 sites on  $\text{MgAl}_2\text{O}_4(100)$  (Figure 2f), and 2 sites on  $\text{MgAl}_2\text{O}_4(110)$  (Figure 2g). Overall, this allows us to include a large variety of adsorption sites in our dataset.

On  $\gamma\text{-Al}_2\text{O}_3(100)$ , the preferred adsorption configuration for all metal atoms except Cu is a hollow site between two oxygens (the case of Pd is shown in Figure S2a,b of the Supporting Information), while Cu is in a different hollow site between two different oxygens (shown in Figure S2c of the Supporting Information). The metal atoms coordinate with both Al and O atoms. The DFT-calculated adsorption energies are as follows: Pt ( $E_{\text{ads}} = -4.62$  eV) < Ir ( $E_{\text{ads}} = -4.56$  eV) < Rh ( $E_{\text{ads}} = -3.57$  eV) < Ni ( $E_{\text{ads}} = -3.55$  eV) < Pd ( $E_{\text{ads}} = -2.59$  eV) < Cu ( $E_{\text{ads}} = -1.64$  eV) < Au ( $E_{\text{ads}} = -0.97$  eV) < Ag ( $E_{\text{ads}} = -0.79$  eV). By convention, more negative adsorption energies are stronger. Additional details regarding the geometry of all binding sites in this study can be found in Tables S8–S19 in the Supporting Information.

On  $\gamma\text{-Al}_2\text{O}_3(110)$ , the strongest adsorption site for Au is a hollow site between Al and O atoms (Figure 3a,b), Cu binds in an identical configuration. Ag prefers adsorption in a hollow site between a different pair of Al and O atoms (shown in Figure S3a,b of the Supporting Information). Pd adsorbs to a hollow site, which is close to the adsorption site of Au and Cu (shown in Figure S3c,d of the Supporting Information). Pt prefers a different hollow site (Figure 3c,d), and Ni, Rh, and Ir bind in an identical configuration. The DFT-calculated metal adsorption energies follow Ir ( $E_{\text{ads}} = -3.87$  eV) < Pt ( $E_{\text{ads}} = -3.71$  eV) < Ni ( $E_{\text{ads}} = -3.14$  eV) < Rh ( $E_{\text{ads}} = -2.69$  eV) < Pd ( $E_{\text{ads}} = -2.20$  eV) < Cu ( $E_{\text{ads}} = -1.64$  eV) < Au ( $E_{\text{ads}} = -1.49$  eV) < Ag ( $E_{\text{ads}} = -1.18$  eV). We note that the strong adsorption (Pt, Ni, Rh, and Ir) causes surface restructuring (support atoms come significantly closer to the supported

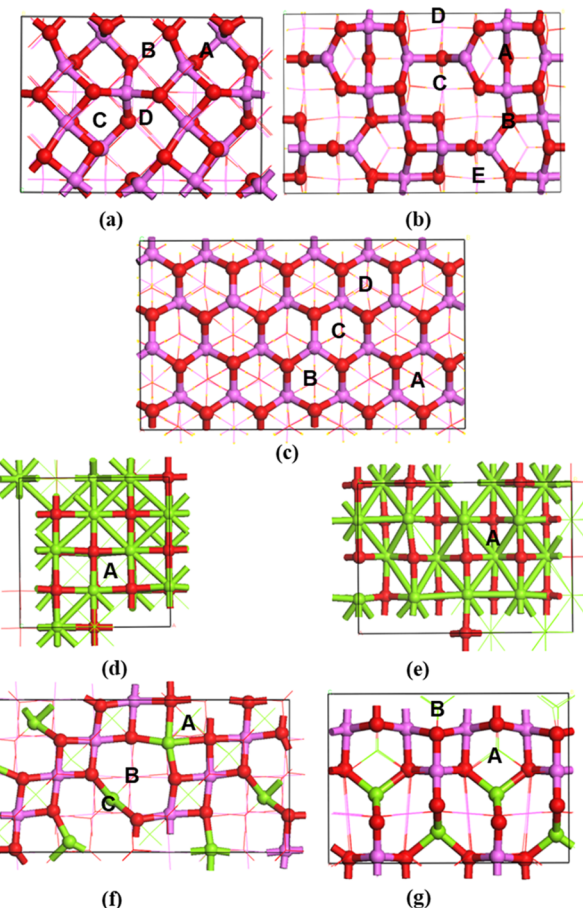


**Figure 2.** Chosen sites on the lowest energy termination of (a)  $\gamma\text{-Al}_2\text{O}_3(100)$ , (b)  $\gamma\text{-Al}_2\text{O}_3(110)$ , (c)  $\gamma\text{-Al}_2\text{O}_3(111)$ , (d) MgO(100), (e) MgO(110), (f)  $\text{MgAl}_2\text{O}_4(100)$ , and (g)  $\text{MgAl}_2\text{O}_4(110)$ . Sites are indicated with capital letters. Only top layers are shown by ball-and-stick, the atoms in the subsurface are shown by a wireframe. Green atoms represent Mg, pink atoms Al, and red atoms O.

metal atom, changing their coordination environment) on the oxide surface (Figure 3e,f).

On  $\gamma\text{-Al}_2\text{O}_3(111)$ , metals bind on a hollow site. The DFT-calculated metal adsorption energies are Ir ( $E_{\text{ads}} = -8.25$  eV) < Ni ( $E_{\text{ads}} = -8.04$  eV) < Rh ( $E_{\text{ads}} = -7.36$  eV) < Pt ( $E_{\text{ads}} = -6.35$  eV) < Cu ( $E_{\text{ads}} = -5.96$  eV) < Pd ( $E_{\text{ads}} = -5.13$  eV) <

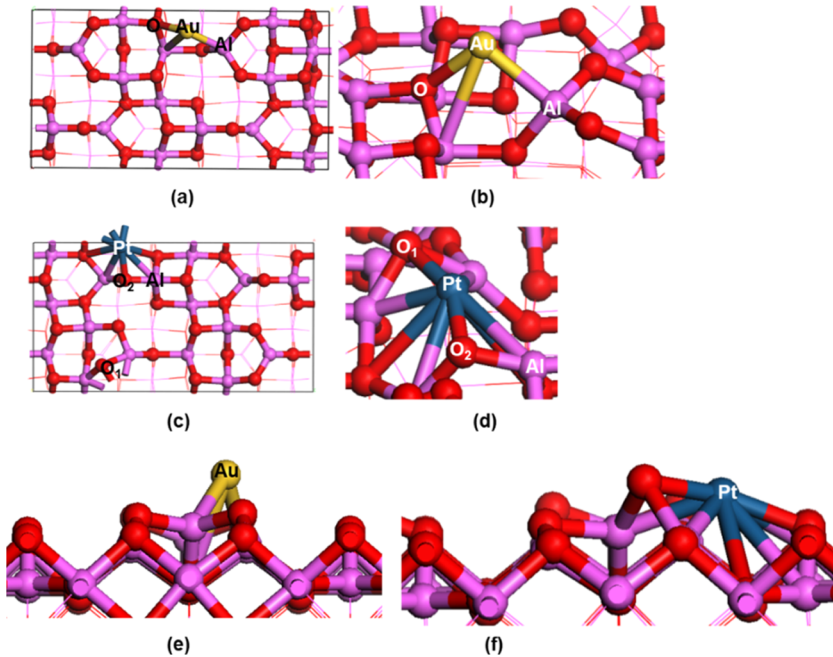


**Figure 3.** Au adsorption on  $\gamma\text{-Al}_2\text{O}_3(110)$  (a) top view, (b) side view; Pt adsorption on  $\gamma\text{-Al}_2\text{O}_3(110)$  (c) top view, (d) side view. Surface restructuring is observed by comparing side views of the  $\gamma\text{-Al}_2\text{O}_3(110)$  support surface when interacting with (e) Au and (f) Pt. Yellow atoms represent Au, blue atoms Pt, pink atoms Al, and red atoms O.

Ag ( $E_{\text{ads}} = -4.54 \text{ eV}$ ) < Au ( $E_{\text{ads}} = -3.75 \text{ eV}$ ). The relatively weakly bound Ag is located on a hollow site (shown in Figure S4a,b of the Supporting Information) and Au binds in an identical configuration. Cu, Pd, Ni, Rh, and Ir bind in the same configuration as Pt (shown in Figure S4c,d of the Supporting Information).

The slab model of MgO(100) yields a highly symmetric support structure. We note that most metals adsorb directly above an oxygen atom and coordinate with several neighboring Mg atoms (represented by Cu in Figure 4a,b). Rh prefers to bind on a hollow site (Figure 4c,d) and Ir binds in an identical configuration. The DFT-calculated adsorption energies are: Pt

( $E_{\text{ads}} = -3.07 \text{ eV}$ ) < Ir ( $E_{\text{ads}} = -2.56 \text{ eV}$ ) < Rh ( $E_{\text{ads}} = -2.03 \text{ eV}$ ) < Ni ( $E_{\text{ads}} = -1.98 \text{ eV}$ ) < Pd ( $E_{\text{ads}} = -1.68 \text{ eV}$ ) < Au ( $E_{\text{ads}} = -1.08 \text{ eV}$ ) < Cu ( $E_{\text{ads}} = -0.98 \text{ eV}$ ) < Ag ( $E_{\text{ads}} = -0.68 \text{ eV}$ ).

On the other stable surface facet of MgO, the (110), most metals strongly bind on a hollow site between two oxygen atoms and coordinate with nearby Mg atoms (shown in Figure S5a,b of the Supporting Information). The most-favorable binding site for Pt is slightly different and prefers to coordinate directly above an oxygen atom with nearby O and Mg atoms (shown in Figure S5c,d of the Supporting Information). The DFT-calculated metal adsorption energy is as follows: Ir ( $E_{\text{ads}} = -4.73 \text{ eV}$ ) < Pt ( $E_{\text{ads}} = -4.48 \text{ eV}$ ) < Ni ( $E_{\text{ads}} = -3.84 \text{ eV}$ ) < Rh ( $E_{\text{ads}} = -3.78 \text{ eV}$ ) < Cu ( $E_{\text{ads}} = -2.57 \text{ eV}$ ) < Pd ( $E_{\text{ads}} = -2.54 \text{ eV}$ ) < Au ( $E_{\text{ads}} = -2.10 \text{ eV}$ ) < Ag ( $E_{\text{ads}} = -2.08 \text{ eV}$ ).

Due to the lower symmetry of  $\text{MgAl}_2\text{O}_4(100)$ , the observed adsorption behavior of different metals varies. Au and Cu bridge the same two nearby Mg atoms (shown in Figure S6 of the Supporting Information), with Ag in an identical binding configuration as Au. Pt binds in a hollow site while coordinating with neighboring Mg, Al, and O atoms (Figure 5a,b). The adsorption configuration of Pd and Ni is the same as Pt. Rh is in a different hollow site between two oxygens and coordinating with nearby Mg and Al atoms (Figure 5c,d). Ir binds in the same configuration. The DFT-calculated metal adsorption energies are: Pt ( $E_{\text{ads}} = -3.89 \text{ eV}$ ) < Ir ( $E_{\text{ads}} = -3.61 \text{ eV}$ ) < Ni ( $E_{\text{ads}} = -2.94 \text{ eV}$ ) < Rh ( $E_{\text{ads}} = -2.76 \text{ eV}$ ) < Au ( $E_{\text{ads}} = -2.38 \text{ eV}$ ) < Cu ( $E_{\text{ads}} = -1.81 \text{ eV}$ ) < Pd ( $E_{\text{ads}} = -1.81 \text{ eV}$ ) < Ag ( $E_{\text{ads}} = -1.21 \text{ eV}$ ).

On  $\text{MgAl}_2\text{O}_4(110)$ , the strongest adsorption site for all metals is similar, which is a hollow site between two nearby oxygens on the surface (shown in Figure S7 of the Supporting Information). DFT-calculated metal adsorption energies are as follows: Ir ( $E_{\text{ads}} = -7.34 \text{ eV}$ ) < Ni ( $E_{\text{ads}} = -6.18 \text{ eV}$ ) < Pt ( $E_{\text{ads}} = -5.77 \text{ eV}$ ) < Rh ( $E_{\text{ads}} = -5.50 \text{ eV}$ ) < Cu ( $E_{\text{ads}} = -4.78 \text{ eV}$ ) < Pd ( $E_{\text{ads}} = -3.74 \text{ eV}$ ) < Ag ( $E_{\text{ads}} = -3.25 \text{ eV}$ ) < Au ( $E_{\text{ads}} = -3.24 \text{ eV}$ ). Although their binding sites are similar, due to

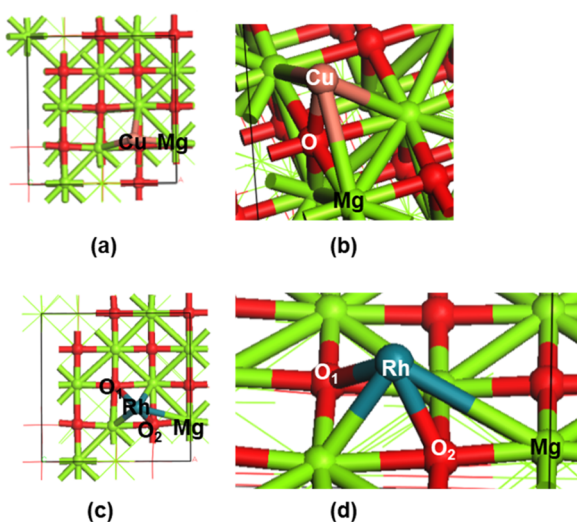


**Figure 4.** Cu adsorption on MgO(100) from (a) top view, (b) side view; Rh adsorption on MgO(100) from the respective (c) top view, (d) side view. Copper atoms represent Cu, blue atoms Rh, green atoms Mg, and red atoms O.

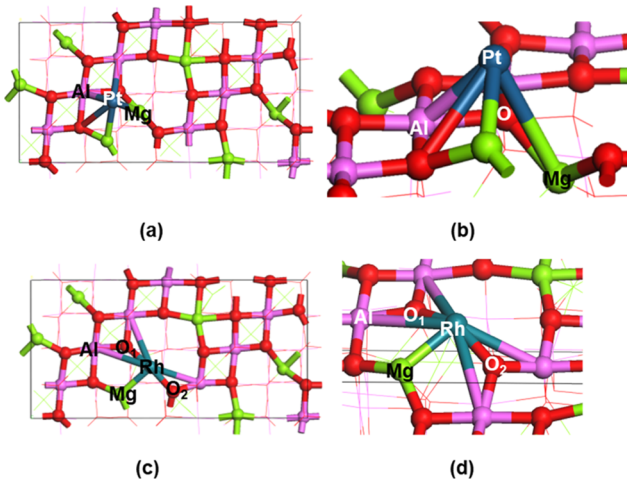


**Figure 5.** Pt adsorption on  $\text{MgAl}_2\text{O}_4(100)$  (a) top view, (b) side view; Rh adsorption on  $\text{MgAl}_2\text{O}_4(100)$  (c) top view, (d) side view. Dark blue atoms represent Pt, light blue Rh, green Mg, pink Al, and red O.

initially high surface energy of  $\text{MgAl}_2\text{O}_4(110)$ , the strong Ir adsorption resulted in a surface restructuring with the Ir bridging two oxygen surface atoms (shown in Figure S7c,d of the Supporting Information).

Overall, a major observation we make from our calculations is that the supported metals move closer to the support oxygens after optimization. For instance, in the case of Ni adsorption on  $\text{MgO}(100)$ , the initial placement of Ni is on a hollow site coordinating with nearby two Mg and two oxygens with average Ni–O distance 2.042 Å (shown in Figure S8a of the Supporting Information). During optimization, the Ni atom moves toward the top site of an oxygen atom with the final Ni–O distance 1.805 Å (shown in Figure S8b of the Supporting Information). This suggests that the metal–oxygen binding is crucial for metal adsorption with strong MSIs inducing surface restructuring to accommodate guest metals on the surface, which we observe in Pt/Ni/Rh/Ir on  $\gamma\text{-Al}_2\text{O}_3(110)$  as well as Ir on  $\text{MgAl}_2\text{O}_4(110)$ . When restructuring, surface oxygen atoms (shown in Figure S7b of the Supporting Information) are pulled toward the supported metal (shown in Figure S7d of the Supporting Information).

In Figure 6, we plot the adsorption energy of metals on their most preferred sites on different oxide supports. We observe for every metal, the adsorption is strongest on  $\gamma\text{-Al}_2\text{O}_3$  and weakest on  $\text{MgO}$ . The metal adsorption on  $\text{MgAl}_2\text{O}_4$  is between  $\gamma\text{-Al}_2\text{O}_3$  and  $\text{MgO}$ . Notably, this trend appears to follow chemical composition where  $\text{MgAl}_2\text{O}_4$  is the combination of  $\text{Al}_2\text{O}_3$  and  $\text{MgO}$ , although the crystal structures of the oxides are different. Because of the similarity in adsorption energy trends for every metal, this suggests that if a metal strongly adsorbs to  $\gamma\text{-Al}_2\text{O}_3$ , it would also adsorb on  $\text{MgO}$  and  $\text{MgAl}_2\text{O}_4$  with a stronger interaction compared to the other metals on the same support. For instance, Ir always binds the strongest among the metals we choose. Finally, the deviation that is observed from the overall trends for Pt (stronger interaction with  $\text{MgO}$  and  $\text{MgAl}_2\text{O}_4$  than Rh) can be attributed to its affinity for Mg atoms that are absent in the case of  $\gamma\text{-Al}_2\text{O}_3$ , as shown in the insets of Figure 6. Overall, these results highlight the role of both the metal and support in governing the overall MSIs.

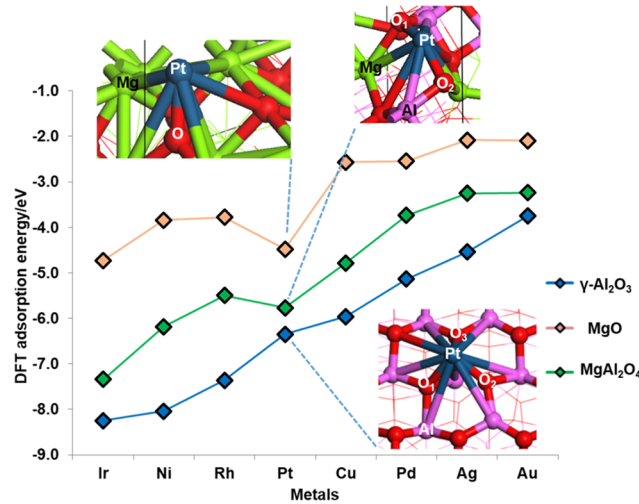


**Figure 6.** DFT-calculated metal adsorption energy for most preferred sites of different transition metals adsorbed on different supports; the structures of Pt adsorption are attached for an insight into the structures. Blue atoms represent Pt, green atoms represent Mg, pink atoms represent Al, and red atoms represent O.

To solidify our conclusions regarding the relationship between the metal–oxygen binding and the MSI, in Figure 7, we plot the adsorption energy of the most preferred site for

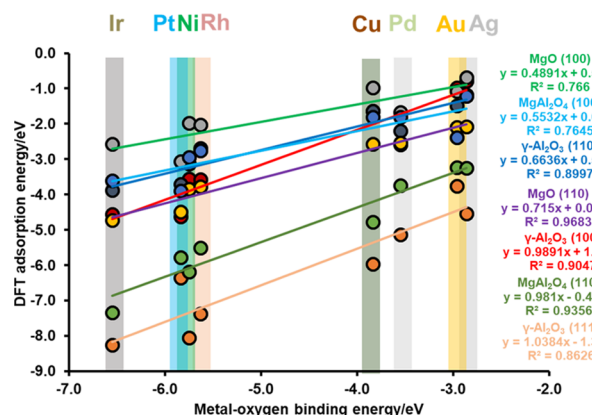


**Figure 7.** Relationships between DFT-calculated metal adsorption energy on each surface facet and metal–oxygen binding energy of the supported SAC.

each metal on several different surface facets versus the metal–oxygen binding energy ( $E_{\text{M}-\text{O}}$ ).  $E_{\text{M}-\text{O}}$  refers to the calculated binding energy of a single metal atom with a single oxygen atom in the gas phase (shown in Table S4 in the Supporting Information). We observe a linear relationship between the metal's adsorption energy on the support and the corresponding  $E_{\text{M}-\text{O}}$ : the stronger the  $E_{\text{M}-\text{O}}$  in the gas phase, the stronger the adsorption energy to the support. On all of the considered facets of  $\gamma\text{-Al}_2\text{O}_3$ , the relationship between metal adsorption energy and  $E_{\text{M}-\text{O}}$  is strong. One of the reasons for this relationship is that except for the relatively weaker binding cases of Au/Cu/Ag on  $\gamma\text{-Al}_2\text{O}_3(110)$  (Figure 3a,b as well as Figure S3a,b of the Supporting Information), all preferred sites for metals on  $\gamma\text{-Al}_2\text{O}_3$  are found to coordinate with a number of oxygen atoms. As a result, the metal–oxygen interaction becomes a major factor for adsorption on  $\gamma\text{-Al}_2\text{O}_3$ , which  $E_{\text{M}-\text{O}}$  characterizes. The correlation between metal adsorption

energy and  $E_{M-O}$  on MgO(100) is weaker due to most metals only coordinating with one oxygen (Figure 4a,b). On MgO(110), every metal participates in strong bonds with two oxygens (shown in Figure S5 of the Supporting Information) and as a result  $E_{M-O}$  works well as a descriptor. On MgAl<sub>2</sub>O<sub>4</sub>(100), Au, Cu (shown in Figure S6 of the Supporting Information), and Ag primarily coordinate with metal centers on the support and the correlation between metal adsorption energy and  $E_{M-O}$  is relatively low. It should be noticed that these specific metals, Au and Ag, have a low affinity for oxygen as shown by the  $E_{M-O}$  descriptor, which justifies their tendency to coordinate with more surface metal atoms than oxygens. On MgAl<sub>2</sub>O<sub>4</sub>(110), the correlation is excellent due to a higher metal–oxygen coordination compared with MgAl<sub>2</sub>O<sub>4</sub>(100) (shown in Figure S7 of the Supporting Information). To summarize,  $E_{M-O}$  is found to be a good descriptor to rationalize MSIs on oxide supports, demonstrating the tendency of a supported metal to interact with surface oxygens.

We now search for a descriptor based on the properties of support, because it is also an important aspect of the adsorption interaction (see our discussion of Figure 6). However, this is not straightforward because the supports display complex structures, which occasionally restructure their surface upon metal adsorption. After screening several support properties (surface energy, band gap, ionization potential, and fermi energy), we identified that the support band gap correlates best with metal adsorption energy. We plot the adsorption energy of metal atoms on the most preferred site versus the band gap of the support in Figure 8. We note that

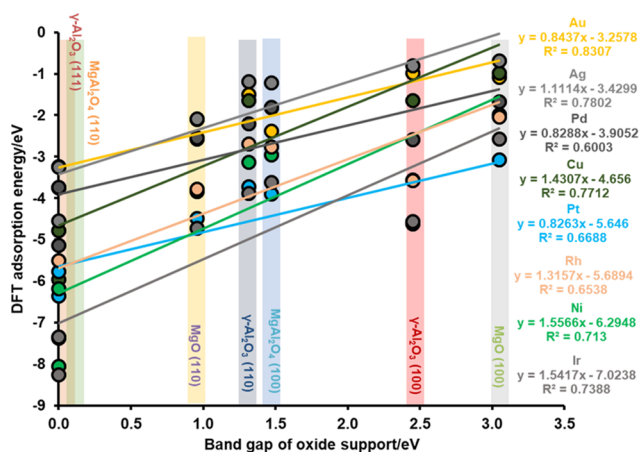


Figure 8. Relationship between DFT metal adsorption energy and band gap of the oxide support.

the smaller the band gap, the stronger the adsorption. This makes sense, because adsorption of metals on supports involves charge transfer.<sup>39</sup> A support with a low band gap can more-easily transfer electron density to form bonds with the adsorbed metal atom, enhancing the adsorption interaction.<sup>64</sup>

The adsorption of metal atoms on the oxide supports involves complex MSIs. As a result, we suspect that additional (potentially nonlinear) factors may play a role in describing adsorption. To explore possibly nonlinear factors related to the MSI, we employ symbolic regression via genetic programming (see the SI section titled “Genetic Programming” for a brief description of the technique), as implemented in Eureqa.<sup>65</sup>

The training set consists of our DFT-calculated adsorption energies, along with several possible physical descriptors, which are obtained from the literature and our own calculations. We calculate the following descriptors using DFT: gas-phase metal–oxygen binding energy ( $E_{M-O}$ ), ionization potential of the support, band gap of the support, Fermi energy of the oxide support, gas-phase HOMO–LUMO gap of the metal, gas-phase Fermi energy of metal, and surface energy of the support (these are listed in Tables S4–S7 of the Supporting Information). In addition to the DFT-calculated parameters, we also investigate coordination numbers (using the bond radii reported in Table S20 of the Supporting Information). We also use a “hypothetical cohesive energy” ( $CE_{hyp}$ ) described in the SRB model to predict the metal atom’s cohesive energy in SACs.<sup>43,44</sup> This is given in eq 2, where  $CE_{bulk}$  is the experimental cohesive energy for metals in the bulk, CN is the total coordination between the supported metal atom and support;  $CN_{bulk}$  is the metal atom’s coordination number in its own bulk. Because we only investigate FCC metals,  $CN_{bulk}$  is always 12. Inherently, we simulate the cohesive energy of the metal atom on its own metal particle with the same coordination that has on the oxide support.

$$CE_{hyp} = CE_{bulk} \sqrt{\frac{CN}{CN_{bulk}}} \quad (2)$$

We consider the following physical properties for the metal from the literature: experimental bulk cohesive energy,<sup>66</sup> experimental ionization potential,<sup>67</sup> experimental electron affinity,<sup>67</sup> oxidation enthalpy,<sup>39</sup> Van del Waal radius,<sup>68,69</sup> electron configuration,<sup>67</sup> Martynov–Batsanov electronegativity,<sup>39</sup> the covalent radius of a triple bond,<sup>70</sup> the heat of vaporization,<sup>71</sup> and electrical resistivity at 273 K.<sup>67</sup>

To combat overfitting, we take 5 subsamples of the dataset, consisting of only 75% of the total dataset, and use each as separate training sets. Genetic programming is inherently a stochastic process, so we run it multiple times to have confidence in our results. For each training set, we run Eureqa 5 times (25 searches total), halting each search after 2 million generations. The complexity is assessed on the equation generated by the Genetic Algorithm (GA). We plot in Figure S11 of the Supporting Information the Pareto Front (the set of equations for each complexity, which minimizes the error)<sup>72</sup> of equations generated by Eureqa, using the RMSE reported by Eureqa.

The equations generated by Eureqa do not necessarily have their coefficients optimized, as they are generated with a genetic algorithm. To further reduce the error of the best equations found by Eureqa, we optimize their coefficients using the Simplex method of Nelder and Mead<sup>73</sup> as implemented in the *optim* function in R. To ensure accurate estimates of RMSE, we utilize bootstrapping (i.e., sampling with replacement from the dataset). We take a bootstrap sample, and then optimize the coefficients. The RMSE is then recorded and another round of sampling and optimization is performed. We repeat this process of bootstrap sampling and optimization 10 000 times for each function. The results of this method are provided in Tables S21–S30 of the Supporting Information. We find eq 3 to be the best equation in terms of bootstrapped RMSE, equaling 0.69 eV. Finally, we use the whole (unbootstrapped) dataset and optimize its coefficients to generate eq 3. In eq 3,  $E_{ads}$  is metal adsorption energy,  $E_{M-O}$  represents the gas-phase metal–oxygen binding energy of the

supported metal,  $IP_s$  represents the ionization potential of the oxide support, and  $BG_s$  represents the band gap of the oxide support.

$$E_{\text{ads}} = 0.523 * E_{\text{M-O}} + \frac{0.413 * E_{\text{M-O}} - 1.243 * IP_s - 4.147}{4.740 * BG_s + 1.165} + 0.859 \quad (3)$$

The correlation between DFT adsorption energy in our dataset and hypothetical adsorption energy calculated using eq 3 is shown in Figure 9.

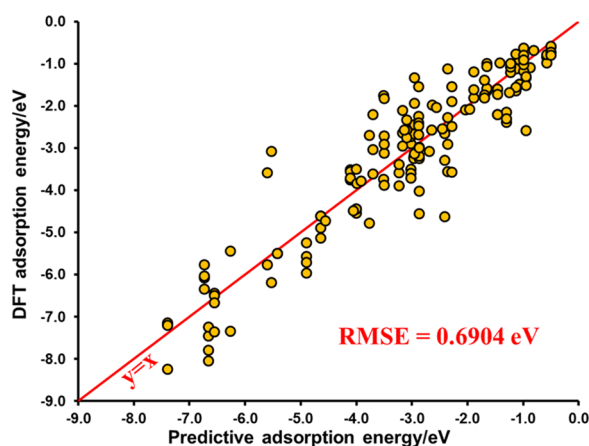


Figure 9. DFT adsorption energy versus predictive adsorption energy calculated by eq 3.

Overall, this equation supports what we elucidated from our DFT calculations. We have already shown that the band gaps of the oxide support ( $BG_s$ ) and metal oxygen binding energy ( $E_{\text{M-O}}$ ) strongly correlate with the metal adsorption energy. Furthermore, the inclusion of the ionization potential of the support ( $IP_s$ ) verifies our conclusion of charge transfer playing an important role in metal adsorption on the support. Examining models recently reported by O'Connor et al.,<sup>39</sup> we find several similar descriptors: the oxide formation enthalpy of the metal (which is similar to our  $E_{\text{M-O}}$ ), the ratio of the LUMO of the support and the metal (we use the support band gap, which is the  $E(\text{LUMO}-\text{HOMO})$ ), and electron affinity of the metal (we use ionization potential of the support) in particular stand out. Our bootstrapped RMSE equals 0.69 eV, which indicates that our model is better suited to a coarse-grained approach to screen a large pool of potential metal–surface pairs before applying a more expensive technique such as DFT.

It is important to compare our single-atom adsorption model with previously developed models in literature. To this end, we compare our model with the work of O'Connor et al.<sup>39</sup> and Iyemperumal et al.<sup>74</sup> O'Connor et al.<sup>39</sup> recently investigated the adsorption of various d-block metals on oxide supports, including  $\text{CeO}_2(111)$ ,  $\text{CeO}_2(110)$ ,  $\text{MgO}(100)$ ,  $\text{TbO}_2(111)$ ,  $\text{ZnO}(100)$ ,  $\text{TiO}_2(011)$ , and  $\alpha\text{-Al}_2\text{O}_3(0001)$ . Several models of metal adsorption were developed, which included nonlinear terms arising from combinations of physical properties such as the coordination of the support metal in the bulk, the electron affinity of the metal, the ionization energy of the metal, oxidation enthalpy of the metal, the LUMO of the metal and support, etc. Iyemperumal et al.<sup>74</sup> also recently investigated the adsorption of various d-block and p-block

atoms on the anatase  $\text{TiO}_2(101)$  surface and developed a simple adsorption model of single atoms to this surface. The best-reported correlations were for the experimental bond dissociation energy of the M–O dimer, the group number and number of d-electrons (both of which are highly correlated), and the d-band center of the adsorbed metal.

The model we have developed as well as the models reported by O'Connor et al.<sup>39</sup> and Iyemperumal et al.,<sup>74</sup> all identified a trend in adsorption with the ability of the adsorbed metal to oxidize. Our descriptor for this is the DFT-calculated M–O dimer bond energy. O'Connor et al.<sup>39</sup> identified the metal's enthalpy of oxide formation, and Iyemperumal et al.<sup>74</sup> identified the tabulated experimental M–O dimer bond energy. In addition, all three models identified an electronic structure descriptor. Our descriptor results from a correlation identified between metal adsorption and the support's band gap. O'Connor et al.<sup>39</sup> showed a dependence on the LUMO of both the metal and the support, and Iyemperumal et al.<sup>74</sup> showed a correlation with the d-band center of the metal. Moreover, we show a correlation with the ionization potential of the support, and similarly O'Connor et al.<sup>39</sup> show a dependence on the electron affinity of the metal. Iyemperumal et al.,<sup>74</sup> on the other hand, show that the electron affinity of the metal has almost no correlation with adsorption on  $\text{TiO}_2$  and a weak correlation with ionization energy. A part of this discrepancy in charge-transfer-based descriptors (i.e., electron affinities and ionization energies) may be due to the differences in the supports: Iyemperumal et al.<sup>74</sup> investigate a reducible support, whereas O'Connor et al.<sup>39</sup> investigate a variety of irreducible and reducible supports, and we investigate irreducible supports.

Other groups have observed similar trends in metal–oxygen binding. Asaduzzaman et al.<sup>75</sup> investigated several 3d transition metals on rutile  $\text{TiO}_2(110)$  and found that the metal–oxygen binding energy to trend with the metal– $\text{TiO}_2$  adsorption energy. The recent work of Dietze et al.<sup>76</sup> focused on the interface of several metals with oxides, represented as two periodic slabs (metal and oxide). It was found that the binding energy of oxygen to the metal surface correlates with the adhesion energy between the metal and oxide surfaces.

Overall, our descriptor selection is well supported by the existing literature. For instance, the inclusion of a term describing the metal's tendency to bind with oxygen<sup>39,74–76</sup> makes physical sense because bonds with oxygen are highly likely to be formed when a metal atom adsorbs to an oxide surface. Our inclusion of an electronic structure descriptor in the form of the band gap is similar to other electronic descriptors reported in literature.<sup>39,74</sup> Finally, the ionization potential of either the metal or support has been used as a descriptor in other models in literature.<sup>39,74</sup> In our case, we use the ionization potential of the support. To summarize, the inclusion of these descriptors makes our model sensitive to (i) the intrinsic tendency for the metal to bind with the oxide (metal–oxygen dimer binding energies) and (ii) the electronic properties of the support (both the ionization potential and band gap of the support).

Stabilizing single metal atoms with a support is a necessity for the creation of stable (i.e., sintering-resistant) SACs. This manifests as a competition between the cohesive energy of the metal atoms (which enhances sintering) and their binding energy with the support (which enhances atomic dispersion). This competition between cohesive energy and binding energy was also suggested as a mechanism for the stabilization of

single Pt atoms on the (100) surfaces of  $\text{CeO}_2$  NPs by Bruix et al.<sup>58</sup> From a thermodynamics perspective, if the strength of the MSI is stronger than the (pure) metal cohesive energy, the single metal atom will energetically prefer adsorption to the support, stabilizing the SAC and resist sintering. This assumption is most applicable in the case of sintering to form large NPs, where a significant fraction of the metal atoms moves far from the metal–support interface such that the CE becomes more important than surface effects (which may be important in stabilizing smaller clusters). We use the SRB model (eq 2) to estimate the hypothetical cohesive energy ( $E_{\text{hyp}}$ ) of the metal atom.

In Figure 10, we plot the adsorption energy of the metal atoms on the different supports versus the  $E_{\text{hyp}}$  of the metal.

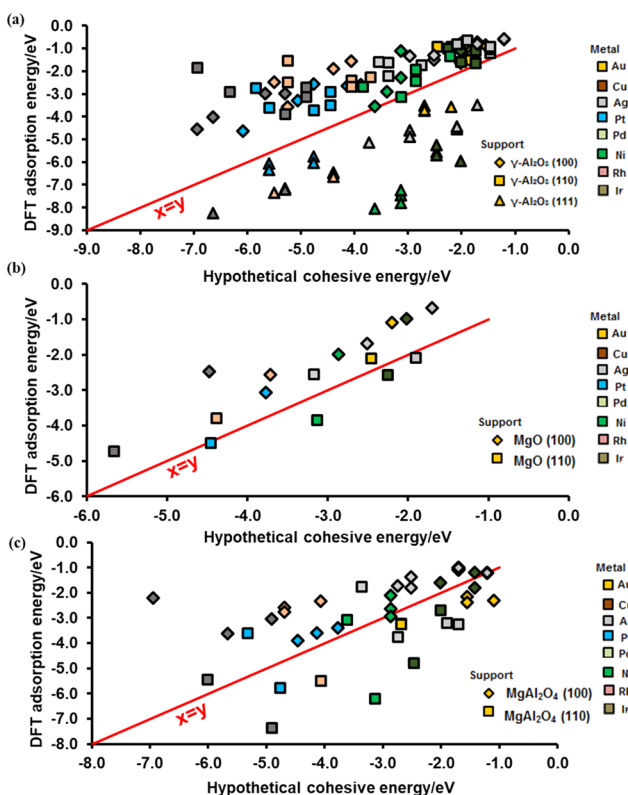


**Figure 10.** DFT adsorption energy vs hypothetical cohesive energy of the supported metal on (a)  $\gamma\text{-Al}_2\text{O}_3$ , (b) MgO, and (c)  $\text{MgAl}_2\text{O}_4$ .

With this formulation, we are able to address the metal's atom preference to interact with the support or with its parent metal (in a cluster/nanoparticle). The red line shows the boundary where the supported metal adsorption energy is equal to SRB-calculated metal cohesive energy. The points below the red line indicate that the adsorption energy is higher than the cohesive energy of a given metal atom, and the corresponding SAC formation is, therefore, suggested to be more favorable. We note that for  $\gamma\text{-Al}_2\text{O}_3$  surface, all data points on (100) and (110) are above the red line, which suggests that stabilizing SACs on these facets may be difficult. However, on (111), all of the considered metals are likely to yield stable SACs, as they are located below the red line (Figure 10a), showing a facet-specific thermodynamic preference for the formation of SACs. We notice that Pt and Rh SACs have already been synthesized on  $\gamma\text{-Al}_2\text{O}_3$ .<sup>60,61</sup> Similarly, on MgO, the surface facet plays an important role in stabilizing SACs, and four points fall under

the red line, which are Cu/Ag/Pt/Ni on  $\text{MgO}(110)$ . Au/Pt/Pd/Rh/Ir SACs have been synthesized on  $\text{MgO}$ .<sup>20,53–55,62</sup> It should be noticed that in Figure 10b, Au, Pd, Rh, and Ir on  $\text{MgO}(110)$  are also close to the red line, validating our predictions. On  $\text{MgAl}_2\text{O}_4$ , most of the data points for (110) surface facet sites are under the red line, suggesting that  $\text{MgAl}_2\text{O}_4(110)$  could also be a good support for the formation of SACs (Figure 10c). Indeed, the Ir SAC has already been synthesized on  $\text{MgAl}_2\text{O}_4$ .<sup>63</sup> Overall, Figure 10 demonstrates that high-energy oxide surface facets are required to stabilize single metal atoms and overcome their thermodynamic tendency to segregate and form nanoparticles. This result demonstrates the complexity of experimentally synthesizing SACs, since typically high-energy surface facets have the tendency to adsorb molecules, such as water that is present on the environment, and alter their surface properties (e.g., acid/base and catalytic properties as in the case of  $\gamma\text{-Al}_2\text{O}_3$ ).<sup>78</sup> These results suggest that the comparison between the metal atom cohesive energy and the adsorption energy on the support could be used as a first screening tool for hypothesizing the stability of SACs.

## CONCLUSIONS

In this work, we apply DFT and statistical methods to a series of transition-metal atoms (Au, Cu, Ag, Pt, Pd, Ni, Rh, and Ir) supported on low-index surface facets of  $\gamma\text{-Al}_2\text{O}_3$ , MgO, and  $\text{MgAl}_2\text{O}_4$  on a variety of sites to determine descriptors for adsorption. Based on our DFT calculations, we identify two primary descriptors for MSIs: the binding energy of the metal–oxygen complex in the gas phase and the band gap of the oxide support. By combining DFT calculations and a thorough statistical learning approach, we develop a mathematical model that is able to estimate MSIs in SACs. Moreover, we introduce a thermodynamic stability metric for the synthetic accessibility of a number of SACs by comparing the DFT adsorption energy with a hypothetical metal atom cohesive energy (the tendency of the metal to form clusters than being atomically dispersed on the support). Our computational results rationalize experimental observations, elucidate the underlying physics of MSIs, and guide experimentalists for the synthesis of SACs.

## ASSOCIATED CONTENT

### Supporting Information

The Supporting Information is available free of charge on the ACS Publications website at DOI: 10.1021/acs.iecr.9b04068.

Structure of surface facets. Pd and Cu adsorption on  $\gamma\text{-Al}_2\text{O}_3(100)$ ; Ag and Pd adsorption on  $\gamma\text{-Al}_2\text{O}_3(110)$ ; Ag and Pt adsorption on  $\gamma\text{-Al}_2\text{O}_3(111)$ ; Rh and Pt adsorption on  $\text{MgO}(110)$ ; Au and Cu adsorption on  $\text{MgAl}_2\text{O}_4(100)$ ; Ag and Ir adsorption on  $\text{MgAl}_2\text{O}_4(110)$ ; Ni adsorption on  $\text{MgO}(100)$ ; example of an equation generated by symbolic regression; RMSE versus the complexity of equations generated by Eureqa; Pareto front; correlation matrix; cell configurations, layers, and lattice constants; data sources used for various physical properties; the calculated metal–oxygen binding energy of the supported metal; the calculated physical properties of the supported metal; calculated ionization potential of the oxide support; calculated physical properties of the oxide support; preferred adsorption site of supported metals on  $\gamma\text{-Al}_2\text{O}_3(100)$ ,

$\gamma$ -Al<sub>2</sub>O<sub>3</sub>(110),  $\gamma$ -Al<sub>2</sub>O<sub>3</sub>(111), MgO(100), MgO(110), MgAl<sub>2</sub>O<sub>4</sub>(100), and MgAl<sub>2</sub>O<sub>4</sub>(110); bonding radii and tables of bootstrapping results ([PDF](#))

## AUTHOR INFORMATION

### Corresponding Author

\*E-mail: [gmpourmp@pitt.edu](mailto:gmpourmp@pitt.edu).

### ORCID

Mudit Dixit: [0000-0001-9456-7806](#)

Giannis Mpourmpakis: [0000-0002-3063-0607](#)

### Notes

The authors declare no competing financial interest.

## ACKNOWLEDGMENTS

This material is based upon work supported by the National Science Foundation under Grant No. 1634880 (CMMI). Computational support was provided by the Center for Research Computing at the University of Pittsburgh, and the Extreme Science and Engineering Discovery Environment, which is supported by the NSF (ACI-1053575).

## REFERENCES

- (1) Cui, X. J.; Li, W.; Ryabchuk, P.; Junge, K.; Beller, M. Bridging homogeneous and heterogeneous catalysis by heterogeneous single-metal-site catalysts. *Nat. Catal.* **2018**, *1*, 385–397.
- (2) Wang, A. Q.; Li, J.; Zhang, T. Heterogeneous single-atom catalysis. *Nat. Rev. Chem.* **2018**, *2*, 65–81.
- (3) Zhang, H.; Liu, G.; Shi, L.; Ye, J. Single-Atom Catalysts: Emerging Multifunctional Materials in Heterogeneous Catalysis. *Adv. Energy Mater.* **2018**, *8*, No. 1701343.
- (4) Ghosh, T. K.; Nair, N. N. Rh1/ $\gamma$ -Al<sub>2</sub>O<sub>3</sub> Single-Atom Catalysis of O<sub>2</sub> Activation and CO Oxidation: Mechanism, Effects of Hydration, Oxidation State, and Cluster Size. *ChemCatChem* **2013**, *5*, 1811–1821.
- (5) Liu, J.; Bunes, B. R.; Zang, L.; Wang, C. Y. Supported single-atom catalysts: synthesis, characterization, properties, and applications. *Environ. Chem. Lett.* **2018**, *16*, 477–505.
- (6) Liu, J. Y. Catalysis by Supported Single Metal Atoms. *ACS Catal.* **2017**, *7*, 34–59.
- (7) Yang, X. F.; Wang, A.; Qiao, B.; Li, J.; Liu, J.; Zhang, T. Single-atom catalysts: a new frontier in heterogeneous catalysis. *Acc. Chem. Res.* **2013**, *46*, 1740–8.
- (8) Flytzani-Stephanopoulos, M. Gold atoms stabilized on various supports catalyze the water-gas shift reaction. *Acc. Chem. Res.* **2014**, *47*, 783–92.
- (9) DeRita, L.; Dai, S.; Lopez-Zepeda, K.; Pham, N.; Graham, G. W.; Pan, X.; Christopher, P. Catalyst Architecture for Stable Single Atom Dispersion Enables Site-Specific Spectroscopic and Reactivity Measurements of CO Adsorbed to Pt Atoms, Oxidized Pt Clusters, and Metallic Pt Clusters on TiO<sub>2</sub>. *J. Am. Chem. Soc.* **2017**, *139*, 14150–14165.
- (10) Hu, P.; Huang, Z.; Amghouz, Z.; Makkee, M.; Xu, F.; Kapteijn, F.; Dikhtierenko, A.; Chen, Y.; Gu, X.; Tang, X. Electronic metal-support interactions in single-atom catalysts. *Angew. Chem., Int. Ed.* **2014**, *53*, 3418–21.
- (11) Yang, M.; Allard, L. F.; Flytzani-Stephanopoulos, M. Atomically dispersed Au-(OH)x species bound on titania catalyze the low-temperature water-gas shift reaction. *J. Am. Chem. Soc.* **2013**, *135*, 3768–71.
- (12) Qiao, B.; Wang, A.; Yang, X.; Allard, L. F.; Jiang, Z.; Cui, Y.; Liu, J.; Li, J.; Zhang, T. Single-atom catalysis of CO oxidation using Pt1/FeOx. *Nat. Chem.* **2011**, *3*, 634.
- (13) Wang, L.; Zhang, W.; Wang, S.; Gao, Z.; Luo, Z.; Wang, X.; Zeng, R.; Li, A.; Li, H.; Wang, M.; Zheng, X.; Zhu, J.; Zhang, W.; Ma, C.; Si, R.; Zeng, J. Atomic-level insights in optimizing reaction paths for hydroformylation reaction over Rh/CoO single-atom catalyst. *Nat. Commun.* **2016**, *7*, No. 14036.
- (14) Cui, X.; Junge, K.; Dai, X.; Kreyenschulte, C.; Pohl, M. M.; Wohlrab, S.; Shi, F.; Bruckner, A.; Beller, M. Synthesis of Single Atom Based Heterogeneous Platinum Catalysts: High Selectivity and Activity for Hydrosilylation Reactions. *ACS Cent. Sci.* **2017**, *3*, 580–585.
- (15) Wang, J.; Zhao, X.; Lei, N.; Li, L.; Zhang, L.; Xu, S.; Miao, S.; Pan, X.; Wang, A.; Zhang, T. Hydrogenolysis of Glycerol to 1,3-propanediol under Low Hydrogen Pressure over WOx-Supported Single/Pseudo-Single Atom Pt Catalyst. *ChemSusChem* **2016**, *9*, 784–90.
- (16) Guo, X.; Fang, G.; Li, G.; Ma, H.; Fan, H.; Yu, L.; Ma, C.; Wu, X.; Deng, D.; Wei, M.; Tan, D.; Si, R.; Zhang, S.; Li, J.; Sun, L.; Tang, Z.; Pan, X.; Bao, X. Direct, nonoxidative conversion of methane to ethylene, aromatics, and hydrogen. *Science* **2014**, *344*, 616–9.
- (17) Duarte, R. B.; Krumeich, F.; van Bokhoven, J. A. Structure, Activity, and Stability of Atomically Dispersed Rh in Methane Steam Reforming. *ACS Catal.* **2014**, *4*, 1279–1286.
- (18) Moses-DeBusk, M.; Yoon, M.; Allard, L. F.; Mullins, D. R.; Wu, Z.; Yang, X.; Veith, G.; Stocks, G. M.; Narula, C. K. CO oxidation on supported single Pt atoms: experimental and ab initio density functional studies of CO interaction with Pt atom on theta-Al<sub>2</sub>O<sub>3</sub>(010) surface. *J. Am. Chem. Soc.* **2013**, *135*, 12634–45.
- (19) Gu, X.-K.; Qiao, B.; Huang, C.-Q.; Ding, W.-C.; Sun, K.; Zhan, E.; Zhang, T.; Liu, J.; Li, W.-X. Supported Single Pt1/Au1 Atoms for Methanol Steam Reforming. *ACS Catal.* **2014**, *4*, 3886–3890.
- (20) Abbet, S.; Sanchez, A.; Heiz, U.; Schneider, W. D.; Ferrari, A. M.; Pacchioni, G.; Rösch, N. Acetylene Cyclotrimerization on Supported Size-Selected Pdn Clusters (1 ≤ n ≤ 30): One Atom Is Enough! *J. Am. Chem. Soc.* **2000**, *122*, 3453–3457.
- (21) Sun, S. H.; Zhang, G. X.; Gauquelin, N.; Chen, N.; Zhou, J. G.; Yang, S. L.; Chen, W. F.; Meng, X. B.; Geng, D. S.; Banis, M. N.; Li, R. Y.; Ye, S. Y.; Knights, S.; Botton, G. A.; Sham, T. K.; Sun, X. L. Single-atom Catalysis Using Pt/Graphene Achieved through Atomic Layer Deposition. *Sci. Rep.* **2013**, *3*, No. 1775.
- (22) Lang, R.; Li, T.; Matsumura, D.; Miao, S.; Ren, Y.; Cui, Y. T.; Tan, Y.; Qiao, B.; Li, L.; Wang, A.; Wang, X.; Zhang, T. Hydroformylation of Olefins by a Rhodium Single-Atom Catalyst with Activity Comparable to RhCl(PPh<sub>3</sub>)<sub>3</sub>. *Angew. Chem., Int. Ed.* **2016**, *55*, 16054–16058.
- (23) Lin, J.; Wang, A.; Qiao, B.; Liu, X.; Yang, X.; Wang, X.; Liang, J.; Li, J.; Liu, J.; Zhang, T. Remarkable performance of Ir1/FeO(x) single-atom catalyst in water gas shift reaction. *J. Am. Chem. Soc.* **2013**, *135*, 15314–7.
- (24) Guan, E.; Gates, B. C. Stable Rhodium Pair Sites on MgO: Influence of Ligands and Rhodium Nuclearity on Catalysis of Ethylene Hydrogenation and H–D Exchange in the Reaction of H<sub>2</sub> with D<sub>2</sub>. *ACS Catal.* **2017**, *8*, 482–487.
- (25) Cheng, N.; Zhang, L.; Doyle-Davis, K.; Sun, X. Single-Atom Catalysts: From Design to Application. *Electrochem. Energy Rev.* **2019**, *1*–35.
- (26) Yan, H.; Su, C. L.; He, J.; Chen, W. Single-atom catalysts and their applications in organic chemistry. *J. Mater. Chem. A* **2018**, *6*, 8793–8814.
- (27) Yan, H.; Cheng, H.; Yi, H.; Lin, Y.; Yao, T.; Wang, C.; Li, J.; Wei, S.; Lu, J. Single-Atom Pd(1)/Graphene Catalyst Achieved by Atomic Layer Deposition: Remarkable Performance in Selective Hydrogenation of 1,3-Butadiene. *J. Am. Chem. Soc.* **2015**, *137*, 10484–7.
- (28) Jones, J.; Xiong, H.; DeLaRiva, A. T.; Peterson, E. J.; Pham, H.; Challa, S. R.; Qi, G.; Oh, S.; Wiebenga, M. H.; Pereira Hernandez, X. I.; Wang, Y.; Datye, A. K. Thermally stable single-atom platinum-on-ceria catalysts via atom trapping. *Science* **2016**, *353*, 150–4.
- (29) Zhu, C.; Fu, S.; Shi, Q.; Du, D.; Lin, Y. Single-Atom Electrocatalysts. *Angew. Chem., Int. Ed.* **2017**, *56*, 13944–13960.
- (30) Campbell, C. T. The energetics of supported metal nanoparticles: relationships to sintering rates and catalytic activity. *Acc. Chem. Res.* **2013**, *46*, 1712–9.

- (31) Zhang, B.; Asakura, H.; Zhang, J.; De, S.; Yan, N. Stabilizing a Platinum Single-Atom Catalyst on Supported Phosphomolybdic Acid without Compromising Hydrogenation Activity. *Angew. Chem., Int. Ed.* **2016**, *55*, 8319–23.
- (32) Campbell, C. T.; Mao, Z. T. Chemical Potential of Metal Atoms in Supported Nanoparticles: Dependence upon Particle Size and Support. *ACS Catal.* **2017**, *7*, 8460–8466.
- (33) Taylor, M. G.; Austin, N.; Gounaris, C. E.; Mpourmpakis, G. Catalyst Design Based on Morphology- and Environment-Dependent Adsorption on Metal Nanoparticles. *ACS Catal.* **2015**, *5*, 6296–6301.
- (34) Stamatakis, M.; Christiansen, M. A.; Vlachos, D. G.; Mpourmpakis, G. Multiscale modeling reveals poisoning mechanisms of MgO-supported Au clusters in CO oxidation. *Nano Lett.* **2012**, *12*, 3621–6.
- (35) Campbell, C. T. Catalyst-support interactions: Electronic perturbations. *Nat. Chem.* **2012**, *4*, 597–8.
- (36) Qiao, B. T.; Liang, J. X.; Wang, A. Q.; Xu, C. Q.; Li, J.; Zhang, T.; Liu, J. Y. Ultrastable single-atom gold catalysts with strong covalent metal-support interaction (CMSI). *Nano Res.* **2015**, *8*, 2913–2924.
- (37) Zhang, Z.; Zhu, Y.; Asakura, H.; Zhang, B.; Zhang, J.; Zhou, M.; Han, Y.; Tanaka, T.; Wang, A.; Zhang, T.; Yan, N. Thermally stable single atom Pt/m-Al<sub>2</sub>O<sub>3</sub> for selective hydrogenation and CO oxidation. *Nat. Commun.* **2017**, *8*, No. 16100.
- (38) Liu, J. J. Advanced Electron Microscopy of Metal-Support Interactions in Supported Metal Catalysts. *ChemCatChem* **2011**, *3*, 934–948.
- (39) O'Connor, N. J.; Jonayat, A. S. M.; Janik, M. J.; Senftle, T. P. Interaction trends between single metal atoms and oxide supports identified with density functional theory and statistical learning. *Nat. Catal.* **2018**, *1*, 531–539.
- (40) Campbell, C. T.; Sellers, J. R. Anchored metal nanoparticles: effects of support and size on their energy, sintering resistance and reactivity. *Faraday Discuss.* **2013**, *162*, 9–30.
- (41) Nørskov, J. K.; Bligaard, T.; Rossmeisl, J.; Christensen, C. H. Towards the computational design of solid catalysts. *Nat. Chem.* **2009**, *1*, 37–46.
- (42) Noronha, F. B.; Fendley, E. C.; Soares, R. R.; Alvarez, W. E.; Resasco, D. E. Correlation between catalytic activity and support reducibility in the CO<sub>2</sub> reforming of methane over Pt/Ce<sub>x</sub>Zr<sub>1-x</sub>O<sub>2</sub> catalysts. *Chem. Eng. J.* **2001**, *82*, 21–31.
- (43) Tománek, D.; Mukherjee, S.; Bennemann, K. H. Simple Theory for the Electronic and Atomic-Structure of Small Clusters. *Phys. Rev. B* **1983**, *28*, 665–673.
- (44) Yan, Z.; Taylor, M. G.; Mascarenas, A.; Mpourmpakis, G. Size-, Shape-, and Composition-Dependent Model for Metal Nanoparticle Stability Prediction. *Nano Lett.* **2018**, *18*, 2696–2704.
- (45) Hutter, J.; Iannuzzi, M.; Schiffmann, F.; VandeVondele, J. CP2K: atomistic simulations of condensed matter systems. *Wiley Interdiscip. Rev.: Comput. Mol. Sci.* **2014**, *4*, 15–25.
- (46) Perdew, J. P.; Burke, K.; Ernzerhof, M. Generalized Gradient Approximation Made Simple. *Phys. Rev. Lett.* **1996**, *77*, 3865–3868.
- (47) Grimme, S.; Antony, J.; Ehrlich, S.; Krieg, H. A consistent and accurate ab initio parametrization of density functional dispersion correction (DFT-D) for the 94 elements H-Pu. *J. Chem. Phys.* **2010**, *132*, No. 154104.
- (48) Bengtsson, L. Dipole correction for surface supercell calculations. *Phys. Rev. B* **1999**, *59*, 12301–12304.
- (49) VandeVondele, J.; Hutter, J. Gaussian basis sets for accurate calculations on molecular systems in gas and condensed phases. *J. Chem. Phys.* **2007**, *127*, No. 114105.
- (50) Goedecker, S.; Teter, M.; Hutter, J. Separable dual-space Gaussian pseudopotentials. *Phys. Rev. B* **1996**, *54*, 1703–1710.
- (51) Hartwigsen, C.; Goedecker, S.; Hutter, J. Relativistic separable dual-space Gaussian pseudopotentials from H to Rn. *Phys. Rev. B* **1998**, *58*, 3641–3662.
- (52) Krack, M. Pseudopotentials for H to Kr optimized for gradient-corrected exchange-correlation functionals. *Theor. Chem. Acc.* **2005**, *114*, 145–152.
- (53) Heiz, U.; Sanchez, A.; Abbet, S.; Schneider, W. D. Catalytic Oxidation of Carbon Monoxide on Monodispersed Platinum Clusters: Each Atom Counts. *J. Am. Chem. Soc.* **1999**, *121*, 3214–3217.
- (54) Heiz, U.; Sanchez, A.; Abbet, S.; Schneider, W. D. Tuning the oxidation of carbon monoxide using nanoassembled model catalysts. *Chem. Phys.* **2000**, *262*, 189–200.
- (55) Hoffman, A. S.; Debefeuille, L. M.; Zhang, S. J.; Perez-Aguilar, J. E.; Conley, E. T.; Justl, K. R.; Arslan, I.; Dixon, D. A.; Gates, B. C. Beating Heterogeneity of Single-Site Catalysts: MgO-Supported Iridium Complexes. *ACS Catal.* **2018**, *8*, 3489.
- (56) Stair, P. C. The Concept of Lewis-Acids and Bases Applied to Surfaces. *J. Am. Chem. Soc.* **1982**, *104*, 4044–4052.
- (57) Kostetskyy, P.; Nolan, C. M.; Dixit, M.; Mpourmpakis, G. Understanding Alkane Dehydrogenation through Alcohol Dehydration on  $\gamma$ -Al<sub>2</sub>O<sub>3</sub>. *Ind. Eng. Chem. Res.* **2018**, *57*, 16657–16663.
- (58) Di'ez, V. K.; Apestegui'a, C. R.; Di Cosimo, J. I. Acid–base properties and active site requirements for elimination reactions on alkali-promoted MgO catalysts. *Catal. Today* **2000**, *63*, 53–62.
- (59) Evans, O. R.; Bell, A. T.; Tilley, T. D. Oxidative dehydrogenation of propane over vanadia-based catalysts supported on high-surface-area mesoporous MgAl<sub>2</sub>O<sub>4</sub>. *J. Catal.* **2004**, *226*, 292–300.
- (60) Lou, Y.; Liu, J. Y. CO Oxidation on Metal Oxide Supported Single Pt atoms: The Role of the Support. *Ind. Eng. Chem. Res.* **2017**, *56*, 6916–6925.
- (61) Van't Blik, H. F. J.; Van Zon, J. B. A. D.; Huizinga, T.; Vis, J. C.; Koningsberger, D. C.; Prins, R. Structure of rhodium in an ultradispersed rhodium/alumina catalyst as studied by EXAFS and other techniques. *J. Am. Chem. Soc.* **1985**, *107*, 3139–3147.
- (62) Sanchez, A.; Abbet, S.; Heiz, U.; Schneider, W. D.; Hakkinen, H.; Barnett, R. N.; Landman, U. When gold is not noble: Nanoscale gold catalysts. *J. Phys. Chem. A* **1999**, *103*, 9573–9578.
- (63) Lu, Y. B.; Wang, J. M.; Yu, L.; Kovarik, L.; Zhang, X. W.; Hoffman, A. S.; Gallo, A.; Bare, S. R.; Sokaras, D.; Kroll, T.; Dagle, V.; Xin, H. L.; Karim, A. M. Identification of the active complex for CO oxidation over single-atom Ir-on-MgAl<sub>2</sub>O<sub>4</sub> catalysts. *Nat. Catal.* **2019**, *2*, 149–156.
- (64) Pacchioni, G. Electronic interactions and charge transfers of metal atoms and clusters on oxide surfaces. *Phys. Chem. Chem. Phys.* **2013**, *15*, 1737–57.
- (65) Schmidt, M.; Lipson, H. Distilling free-form natural laws from experimental data. *Science* **2009**, *324*, 81–5.
- (66) Kittel, C. *Introduction to Solid State Physics*, 8th ed.; Wiley: Hoboken, NJ, 2005; p xix, 680 p.
- (67) Haynes, W. M. *CRC Handbook of Chemistry and Physics*, 92nd ed.; CRC Press: Hoboken, 2011.
- (68) Hu, S. Z.; Zhou, Z. H.; Robertson, B. E. Consistent approaches to van der Waals radii for the metallic elements. *Z. Kristallogr.* **2009**, *224*, 375–383.
- (69) Mantina, M.; Chamberlin, A. C.; Valero, R.; Cramer, C. J.; Truhlar, D. G. Consistent van der Waals radii for the whole main group. *J. Phys. Chem. A* **2009**, *113*, 5806–12.
- (70) Pyykkö, P.; Riedel, S.; Patzschke, M. Triple-bond covalent radii. *Chem. – Eur. J.* **2005**, *11*, 3511–20.
- (71) Zhang, Y. M.; Evans, J. R. G.; Yang, S. F. Corrected Values for Boiling Points and Enthalpies of Vaporization of Elements in Handbooks. *J. Chem. Eng. Data* **2011**, *56*, 328–337.
- (72) O'Reilly, U.-M. *Genetic Programming Theory and Practice II*; Springer: New York, 2005; p xiv, 320 p.
- (73) Nelder, J. A.; Mead, R. A Simplex-Method for Function Minimization. *Comput. J.* **1965**, *7*, 308–313.
- (74) Iyemperumal, S. K.; Pham, T. D.; Bauer, J.; Deskins, N. A. Quantifying Support Interactions and Reactivity Trends of Single Metal Atom Catalysts over TiO<sub>2</sub>. *J. Phys. Chem. C* **2018**, *122*, 25274–25289.
- (75) Asaduzzaman, A. M.; Kruger, P. Adsorption of 3d Transition Elements on a TiO<sub>2</sub>(110) Surface. *J. Phys. Chem. C* **2008**, *112*, 19616–19619.

(76) Dietze, E. M.; Plessow, P. N. Predicting the Strength of Metal–Support Interaction with Computational Descriptors for Adhesion Energies. *J. Chem. Phys. C*. **2019**, *123*, 20443–20450.

(77) Brux, A.; Lykhach, Y.; Matolinova, I.; Neitzel, A.; Skala, T.; Tsud, N.; Vorokhta, M.; Stetsovych, V.; Sevcikova, K.; Myslivecek, J.; Fiala, R.; Vaclavu, M.; Prince, K. C.; Bruyere, S.; Potin, V.; Illas, F.; Matolin, V.; Libuda, J.; Neyman, K. M. Maximum noble-metal efficiency in catalytic materials: atomically dispersed surface platinum. *Angew. Chem., Int. Ed.* **2014**, *53*, 10525–30.

(78) Dixit, M.; Kostetskyy, P.; Mpourmpakis, G. Structure–Activity Relationships in Alkane Dehydrogenation on  $\gamma$ -Al<sub>2</sub>O<sub>3</sub>: Site-Dependent Reactions. *ACS Catal.* **2018**, *8*, 11570–11578.